ECV Uncertainty Budget (EUB)

glaciers cci

Prepared by:	Glaciers_cci consortium
Contract:	4000127593/19/I-NB
Name:	Glaciers_cci+_ph2_D2.3_EUB
Version:	1.1
Date:	30.11.2023

Contact:
Frank Paul
Department of Geography
University of Zurich
frank.paul@geo.uzh.ch

Technical Officer:
Anna Maria Trofaier
ESA Climate Office

UNIVERSITY OF OSLO

University of Zurich[UZH]

UCL Mullard Space Science Laboratory

GAMMA REMOTE SENSING

enveo

Document status sheet

Version	Date	Changes	Approval
1.0	10.10.2023	Initial draft	
1.1	30.11.2023	Consortium input included	

The work described in this report was done under ESA contract 4000127593/19/I-NB. Responsibility for the contents resides with the authors who prepared it.

Author team:
Andreas Kääb, Désirée Treichler (GUIO), Thomas Nagler, Jan Wuite (ENVEO), Tazio Strozzi, Andreas Wiesmann (Gamma), Frank Paul (GIUZ), Lin Gilbert (UCL)

Glaciers_cci Technical Officer at ESA:
Anna Maria Trofaier

Related documents

Acronym	Title	Document reference	Date
[RD1]	UCR CCI	Uncertainty Characterisation Reportv2	11.11.2016
[RD2]	ATBD CCI+	Algorithm Theoretical Basis Document	10.10.2020
[RD3]	PVIR CCI+	Product Validation and Intercomparison Report	21.12.2021
[RD4]	EUBv2	CCI+ Phase 1 ECV Uncertainty Budget (EUB) v2	17.03.2022

Table of Contents

1. Purpose of this document

This document provides a description of the ECV uncertainty budget for the new algorithms developed in Glaciers_cci+ Phase 2 (see [RD1] for the algorithms of Glaciers_cci+ Phase 1) and documented in its ATBD [RD2]. This document is thus also structured along the new sensors and products created in Glaciers_cci+ Phase 2, i.e. we do not repeat here details from the related Phase 1 documents.

According to the Statement of Work (SoW), the Glaciers_cci+ EUB shall present major sources of error and estimate uncertainties according to each step of the retrieval process. Moreover, potential sources of error from ancillary data and external processes shall be investigated. Finally, sources of errors that are difficult or impractical to quantify shall be investigated.

We thus cover for each product and algorithm of the ATBD [RD2] the following aspects:

- Major error sources
- Uncertainties per processing step
- Other uncertainties

This first version of the EUB contained rather general, qualitative uncertainty descriptions, based on insights from previous studies. The document will be updated once the products have been created.

2. New sensors

2.1 Glacier mapping with Landsat 9

For the comparison of glacier mapping results using Landsat 9 with those from Landsat 8 and Sentinel-2 we focus on clean ice mapping without further manual corrections. We also do not consider geolocation issues (see Section 2.2) and derive glacier areas directly for the individual polygons. Due to limited availability of reference datasets, we also do not provide errors and a bias but relative uncertainties, i.e. relative area differences for the analysed sensors. Native areas for the selected glacier polygons are calculated at the spatial resolution of the sensor rather than being resampled to a common resolution (of 10 or 15 m).

2.1.1 Major error sources

The above constraints limit area differences to the application of a different threshold applied to the band ratio image. These are expected due to different atmospheric conditions after 8 days (for Landsat 8), sensor calibration, revised gain and offset values, etc. The thresholds to be applied for the automated glacier mapping will thus differ slightly for the different sensors.

2.1.2 Uncertainties per processing step

The purpose of this comparison is to determine the uncertainties for this processing step. They will be reported in the next version (v2) of this document.

2.1.3 Other uncertainties

As snow cover is also mapped by the band ratio method, only scenes without snow cover off glaciers can be used for this comparison. Otherwise one would only detect the change in snow cover over an 8-day period (which could be large enough to be detected).

2.2 Geometric consistency Landsat / Sentinel-2

According to Rengarajan et al. (2020), the geolocation difference between Landsat and Sentinel-2 has been corrected by using GCPs derived for the Sentinel-2 Global Reference Image (i.e. the Landsat scenes have been reprocessed). With this investigation we will check for a couple of regions if this is indeed the case.

2.2.1 Major error sources

Major error sources for geolocation in relative terms (between two sensors) are related to (1) a different DEM is used for the orthorectification and (2) different ground control points (GCPs) are used. In absolute terms, also the spatial resolution of the DEM, its quality (e.g. artefacts or data voids) and timing can shift pixels to a place where they should not be. For example, if 10 m Sentinel-2 images are orthorectified with a 90 m DEM from 2000, not only glacier-free terrain will be displaced irregularly, but also glaciers due to their strong surface lowering over time (Kääb et al. 2016).

2.2.2 Uncertainties per processing step

The purpose of this comparison is to determine the uncertainties for this processing step. They will be reported in the next version (v2) of this document.

2.2.3 Other uncertainties

We will likely detect further sources of uncertainty during data processing and analysis. They will be reported in version 2 (v2) of this document.

2.3 Sentinel-3

Sentinel-3 data was used in the first phase of the Glaciers CCI+ project, documented in the phase 1 ATBD and EUB. Since phase 1 the Thematic Land Ice product has been released, and will be used for phase 2. The thematic product comes from a surface-specific land ice processing chain, with an extended radar window for waveform processing, and an improved slope model. These changes improve retrieval rates of surface height measurements, especially during the transition from ocean to land, and accuracy of height measurements. Preliminary assessment is available in the test dataset report, European Space Agency (2022).

2.3.1 Major error sources

As with all radar altimetry, the major sources of error come from the three sources - satellite location and orientation, corrections due to atmospheric effects on the radar pulse round-trip time and surface effects such as volume scattering from within the radar footprint. Of these, the most important is slope correction, where the echoing point of the radar pulse is offset from nadir when over sloping terrain. Although the thematic product's new slope model aims to improve calculation of the offset, a validation campaign with the aircraft-mounted scanning laser altimeter from Operation IceBridge was performed in 2021. This characterised uncertainties in different slope ranges, using data over northwest Greenland from 2017. Its results were reported in the Sentinel 3 Mission Performance Centre annual report (CLS et al. 2021).

2.3.2 Uncertainties per processing step

Input: Individual Sentinel-3 elevation uncertainties are taken from the slope-dependent look-up table (CLS et al., 2021).
Datapoint migration to reference point: Migration uses the difference in elevation between two locations as given by the Arctic DEM. Elevation uncertainty is approximately 0.2m according to Noh and Howat, 2015. Both instances of this uncertainty are summed in quadrature with the input uncertainty to get the total uncertainty on each element of the timeseries.
Interpolation: Missing reference points will be filled by universal Kriging, where the uncertainty is supplied by the algorithm as a variance field.
Geographical averaging: Uncertainty is taken as the RMSE of the inputs.
Elevation change rate: The change rate uncertainty derived from a timeseries comes from two sources - input and modelling. The input component is the RMSE of the datapoints in the timeseries, divided by the time window. The modelling component is the standard deviation of the model fitted to the timeseries. Both components summed in quadrature give the total uncertainty.

2.3.3 Other uncertainties

The uncertainty per slope range table derived during the validation campaign incorporates all sources of uncertainty. In particular, as the comparison was with a laser altimeter, radar penetration of the ice is incorporated.

2.4 Cryosat-2 swath mode

CryoSat-2 data was previously used in phase 1 of the Glaciers CCI+ project, documented in the phase 1 ATBD and EUB. However, the novel swath processing method includes a new treatment of uncertainties.

2.4.1 Major error sources

Every swath datapoint is given an uncertainty value in metres. This is derived from a look-up table, which incorporates 6 quality variables – power in decibels, coherence, distance to POCA, along- and across- track slope, and DEM roughness. To make the look-up table a subset of the swath elevation points is binned into a six-dimensional array using all combinations of the swath quality variables. In each bin the uncertainty is calculated as the 95th percentile of the standard deviation of the elevation differences to an auxiliary altimetry dataset. In general this is a conservative estimate of the uncertainty, but does not guarantee that the point is not an outlier. For Greenland the reference DEM was the Arctic DEM and the uncertainty calibration dataset was ICESat-2's ATL06 product (Land Ice Height) from 2021.

The gridded swath product is derived from the point swath product and the uncertainty per grid cell is derived from the point uncertainty, which is propagated by taking spatial autocorrelation into account within each region. In this case the region is Greenland.

2.4.2 Uncertainties per processing step

Inputs: Input uncertainties are supplied as part of the product, for both point and gridded products.
Point product timeseries: Uncertainty per cell within a given timespan is taken as the RMSE of the inputs.
Gridded product timeseries: These are created by stacking the inputs, which are supplied with their associated uncertainties.
Interpolation: Missing timeseries points will be filled from known timeseries on the same glacier by universal Kriging, where the uncertainty is supplied by the algorithm as a variance field.
Geographical averaging: Uncertainty is taken as the RMSE of the inputs.
Elevation change rate: The change rate uncertainty derived from a timeseries comes from two sources - input and modelling. The input component is the RMSE of the datapoints in the timeseries, divided by the time window. The modelling component is the standard deviation of the model fitted to the timeseries. Both components summed in quadrature give the total uncertainty.

2.4.3 Other uncertainties

The swath data was calculated from CryoSat-2 baseline C products, which corrected a problem in baseline B with roll bias - the reported satellite roll angle was not correct. Analysis (Gourmelen et al, 2018) has found a residual error of approximately 0.007° and if uncorrected, this directly translates in an offset of 87 m in geolocation in the across track direction, and in a vertical offset of 0.01 m at nadir and of 1.60 m at the edge of the footprint, of the elevation retrieval. This is incorporated within the look-up table figures.

2.5 ICESat-2

The Advanced Topographic Laser Altimeter System (ATLAS) on board ICESat-2 is a photon counting lidar. Geolocated and time-tagged photon events are processed into higher-level products based on ground surface type. Land ice products are assembled into height timeseries in product ATL11. From this a gridded DEM, ATL14, and a set of time-tagged height changes to the DEM, ATL15, are derived. Uncertainties are derived at each processing step.

2.5.1 Major error sources

ATL11 provides a combined error estimate per measurement. This has two components. The per-point uncertainties related to the accuracy of the lidar range measurement and the reference surface are uncorrelated between points. There are also systematic uncertainties, from measurement geolocation and satellite radial orbit errors.

ATL14 and ATL15 are based on models of the ATL11 inputs. The dominant error source in ATL11 is the effect of geolocation errors over sloping surfaces. The per-point uncertainties of the inputs are retained, while the systematic uncertainties are recalculated in the modelling process by adding terms for parameter biases (e.g. pointing error and slope error) and smoothing constraints on the model.

2.5.2 Uncertainties per processing step

Inputs: Uncertainties are supplied with each input measurement.
Grid cell averaging: ATL14 will be averaged to match the grid resolution of ATL15, with the uncertainty per averaged cell taken as the RMSE of the input uncertainties.
Combination: Total uncertainty for each point in the assembled timeseries comes from the averaged ATL14 uncertainty summed in quadrature with the input ATL15 datapoint uncertainty.
Geographical averaging: Uncertainty is taken as the RMSE of the inputs.
Elevation change rate: The change rate uncertainty derived from a timeseries comes from two sources - input and modelling. The input component is the RMSE of the datapoints in the timeseries, divided by the time window. The modelling component is the standard deviation of the model fitted to the timeseries. Both components summed in quadrature give the total uncertainty.

2.5.3 Other uncertainties

Within the ATL14 and ATL15 modelling processes, a term for local variation within the modelling area, e.g. from localised differences in surface processes, or other unknowns, is added. This incorporates variations not accounted for by the per-point and systematic uncertainties.

2.6 SAOCOM A/B

2.6.1 Major error sources

In phase 2 of the project we test and exploit the use of SAOCOM L-Band in combination with Sentinel-1 C-Band SAR for retrieving and improving glacier surface velocity using both offset tracking (OT) and InSAR algorithms. The InSAR and offset tracking processing lines de-

veloped for other SAR sensors (e.g. Sentinel-1, TerraSAR-X) in Glaciers_cci have been adapted to accommodate SAOCOM as well as the combination of SAOCOM and Sentinel-1. Sources of errors and uncertainties, both internal (i.e. algorithm dependent) and external, as well as methods for accuracy determination were discussed in detail in [RD1] and [RD4] and are here summarised with a focus on the SAOCOM constellation.

Offset-based methods are sensitive to all sources that contribute to image misalignment between two acquisitions in both the slant-range and azimuth directions. Furthermore, the topographic component mainly impacts the slant-range offset measurements, whereas the dominating atmospheric error component is due to ionospheric scintillations, causing spatially varying azimuth shifts. Errors in InSAR derived products can arise from several sources:

- Decorrelation and random phase noise
- Baseline errors
- Phase unwrapping errors
- Phase calibration errors

2.6.2 Uncertainties per processing step

Inaccuracies in the annotated state vectors of the input SLC images introduce errors in the baseline calculation, which in turn leaves a residual phase contribution in the interferogram. This is more of a concern in the case of SAOCOM as compared to Sentinel-1 because of the lower quality orbits of SAOCOM. The use of interferometry requires stringent orbit control, with pointing and timing/synchronisation between interferometric pairs. This is in particular relevant for burst-mode interferograms (e.g. TOPS acquisitions). This condition is met for Sentinel-1, which has a small orbital tube of 100 m and in TOPS mode acquisition performs a synchronisation at the beginning of the IW data takes with an accuracy better than 3 ms (Prats et al., 2015). Because SAOCOM has a much larger orbital tube and generally no burst synchronisation in TOPSAR mode we use SAOCOM StripMap (SM) data. Therefore, in contrast to Sentinel-1 TOPSAR, phase jumps are not a concern.

In the final step of the InSAR processing chain, line-of-sight (LOS) velocity maps from different viewing geometries (e.g. crossing orbits SAOCOM-SAOCOM or SAOCOM-Sentinel-1) that have been generated with SAR interferometry are combined through a least-squares inversion in order to retrieve the 2D surface velocity. To account for interferometric processing uncertainties, phase variances from random phase noise and phase calibration are summed up and used as weights of the input data in the least-squares inversion. With an uncertainty estimate available for each line-of-sight observation, the resulting 2D velocity errors can be estimated as part of the velocity inversion.

2.6.3 Other uncertainties

In case that only one LOS velocity map is available or if there are gaps in the interferometrically derived ice velocity from one LOS direction a combined use of interferometric velocity measurements with offset-tracking derived flow directions can be used. The flow directions, in that case, are then typically derived from a multi-annual offset-tracking velocity map (if available) and are a source of additional uncertainty, however this is generally considered to be very small.

2.7 ICEYE SAR

2.7.1 Major error sources

The relevant sources of uncertainty of the ice surface velocity products derived from intensity cross-correlation of SAR and optical satellite images and from SAR interferometry (InSAR) as well as the methods for accuracy determination were discussed in detail in the CCI Uncertainty Characterization Report (UCR) and in the CCI+ Phase 1 ECV Uncertainty Budget (EUB). In the following, we only discuss peculiarities of the ICEYE constellation impacting on the uncertainty characterization.

In general, the InSAR and offset tracking processing lines developed for other sensors in glaciers_cci could be readily adapted to the ICEYE data. The ICEYE orbit control was not optimal for the first launched satellites. This changed with the launch of the ICEYE X6 satellite (in autumn 2020) with short baselines (i.e. < 200 m) at high latitudes within a few days, but also including a drifting to considerably large values after a few days. With large baselines the InSAR phase sensitivity to topography gets larger and spatial decorrelation increases. InSAR is therefore typically employed with short-baseline interferograms. In addition, with large baselines stereo offsets become greater.

Furthermore, we observed that the Noise Equivalent Sigma Zero (NESZ) of the ICEYE SAR data is high, especially in the very near and very far range of the scene. As a consequence, the coherence tends to reduce over surfaces with low backscatter. However, the quality of the ice velocity products determined with offset-tracking over glaciers is not affected by this effect.

2.7.2 Uncertainties per processing step

For further details about uncertainties of the glacier flow velocity product see [RD4].

2.7.3 Other uncertainties

For further details about other uncertainties of the glacier flow velocity product see [RD4].

3. New products

3.1 Glacier length changes from Keyhole images

In the following we refer only to the assessment of length changes. For error sources and uncertainties related to the processing of Corona images see Section 2.4 in the EUBv2 from Glaciers_cci+ Phase 1 [RD4].

3.1.1 Major error sources

The two major error sources for the determination of length changes from multi-temporal satellite images are (1) imperfect co-registration and (2) interpretation uncertainties. As we do not co-register the individual images to a master image, but use them as provided by the space agencies or our own processing, the geolocation uncertainty un_{geo} of the individual scenes adds up independently and largely depends on pixel size. For a geolocation uncertainty of one pixel, the related uncertainty when length changes are determined between two images with the respective spatial resolutions res_1 and res_2, can be calculated as (Hall et al. 2003):

$$un_{geo} = \sqrt{res_1^2 + res_2^2}$$

The resulting uncertainties for different sensor combinations are summarized in Table 3.1. Additionally, positioning of the points marking the terminus can also only be performed with an uncertainty of one pixel. The related uncertainty of the terminus un_{term} for two measurements is (Williams et al. 1997):

$$un_{term} = \sqrt{res_1^2 + res_2^2}$$

As both uncertainties are independent, the total uncertainty un_{tot} can be calculated as:

$$un_{tot} = \sqrt{un_{geo}^2 + un_{term}^2}$$

which is for measurements with sensors of the same spatial resolution res: $un_{tot} = 2 * res$.

Table 3.1: Uncertainties of un_{geo}/un_{term} for different sensor combinations and total uncertainty.

Sensor	Resolution (m)	Combination with 10 m	Combination with 15 m	Combination with 30 m	Total uncertainty 10 m	Total uncertainty 15 m	Total uncertainty 30 m
Corona	10	14.1	18.0	31.6	20	25.5	44.7
Landsat TM	30	31.6	33.5	42.4	44.7	47.4	60
Landsat pan	15	18.0	21.2	33.5	25.5	30	47.4
Sentinel-2	10	14.1	18.0	31.6	20	25.5	44.7

3.1.2 Uncertainties per processing step

The length change product will be derived by digital intersection of a centreline with digitized extents from different point in time. Depending on the sensors used, the above equations will be applied to determine the uncertainty.

3.1.3 Other uncertainties

The centreline length changes might differ from changes calculated from a set of parallel lines of sight or other techniques.

3.2 Glacier facies mapping

3.2.1 Major error sources

The main contributions to the per-pixel uncertainty of the glacier facies products from optical satellite data are errors coming from the

- satellite signal,
- auxiliary data,
- algorithms for pre-processing and cloud masking,
- classification of glacier facies.

These are described in the following in more detail.

3.2.2 Uncertainties per processing step

Satellite signal

The glacier facies product generation from optical satellite data is based on L1C data of the Sentinel-2A/B and Landsat missions. Uncertainties for an individual scene result from the instrument's noise, the geolocation of the L1C data, and the processing of the raw data to L1C.

To cover the full area of interest, data from overlapping tracks and tiles are needed. For Sentinel-2 data, uncertainties are coming from differences in the spectral reflectances for pixels covered by overlapping satellite data acquired on the same date and time resulting from the tile based preparation of the L1C products. Major uncertainties are also coming from shifts in the geolocation of tiles. These sources for uncertainties are mainly observed for Sentinel-2 L1C data acquired between 2015 and 2021 and generated with the processing baseline versions v2.X and v3.X.

For Landsat data, the spatial coverage of scenes with the same path and row can be shifted about more than 1 km. As time series of the same scene are required to classify the glacier facies, such shifts can introduce uncertainties in the final product. To cover the full area of interest, Sentinel-2 and Landsat scenes of multiple neighbouring tracks are needed, which are acquired on different dates (Figure 3.2.1). Uncertainties introduced by the satellite data are random, and cannot be quantified in a systematic way.

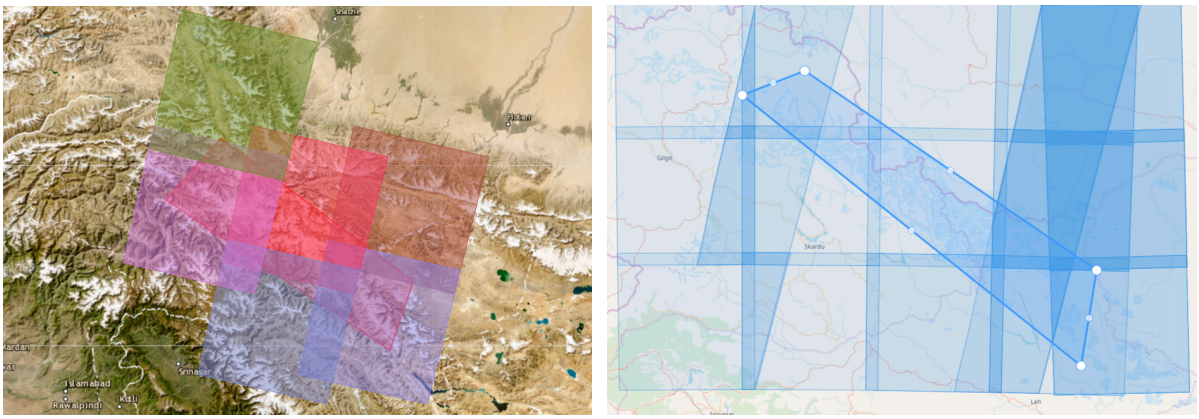

Figure 3.2.1: Schematic overview of Landsat (left) and Sentinel-2 (right) scenes required to cover the glaciers of the Karakoram region.

Auxiliary data

As auxiliary data for the glacier facies retrieval, the following datasets are needed:

- glacier outlines over the area of interest as vector or raster layer,
- a digital elevation model (DEM), and
- gridded atmospheric parameters, including aerosol optical depth at 550 nm, total column of water vapour content in the atmosphere, and total column of ozone in the atmosphere for the time of the image acquisition (optional: a predefined standard atmosphere).

Each of these data sets contributes to the overall uncertainty of the GLF product.

The glacier outlines of the Randolph Glacier Inventory v7.0 (RGI 7.0) for the region South Asia West are used. This data set contains the glacier outlines mapped from high resolution optical satellite data acquired around the year 2000. Any changes in the glacier extent in earlier or later years are not included in this data set, and can thus introduce uncertainties in the GLF products. However, for the accumulation region changes in extent over time are small.

The accuracy of the DEM has a major impact on the processing, especially for regions affected by cast shadow. Four DEMs were investigated over the glaciers in the Karakoram:

1. the Copernicus Global DEM with 30 m pixel spacing (GLO-30) (https://spacedata.copernicus.eu/collections/copernicus-digital-elevation-model, https://doi.org/10.5270/ESA-c5d3d65),
2. the NASA Shuttle Radar Topography Mission (SRTM) DEM version 4.1 with 90 m pixel spacing (SRTM v4.1) (Jarvis et al., 2008),
3. the NSIDC High Mountain Asia DEM with 8 m pixel spacing (https://nsidc.org/data/highmountainasia), and
4. the JAXA ALOS World 3D DEM v3.2 with 30 m pixel spacing (https://www.eorc.jaxa.jp/ALOS/en/dataset/aw3d30/aw3d30_e.htm).

Two of these DEMs, the GLO-30 and the SRTM v4.1 have full spatial coverage over the glaciers in the Karakoram, and have thus been considered for further analyses. In some regions over this area of interest, differences between these two DEMs are in the order of several hundreds of metres (Figure 3.2.2).

After testing the processing with both DEMs, containing each the orthometric height per pixel, the GLO-30 has been selected. Any errors or uncertainties in the DEM have an impact on the following processing steps and thus contribute to the uncertainty of the final GLF product, especially on the GLF detection in cast-shadowed areas.

Atmospheric parameters are taken from the 4th generation of ECMWF Atmospheric Composition Reanalysis data of the Copernicus Atmosphere Monitoring Service (CAMS). This reanalysis data set provides the required atmospheric parameters on a global scale with about 80 km pixel spacing for 60 model levels every 3 hours for the period 2003 to 2022. For more recent dates, the analysis data of the CAMS global forecasts of atmospheric composition are used, which are globally available with a pixel spacing of about 40 km for 60 model levels every 3 hours for the period 2015 until 7th July 2019, 00 UTC, and for 137 model levels since then. When no reanalysis data are available, the standard atmosphere for mid-latitude summer is assumed.

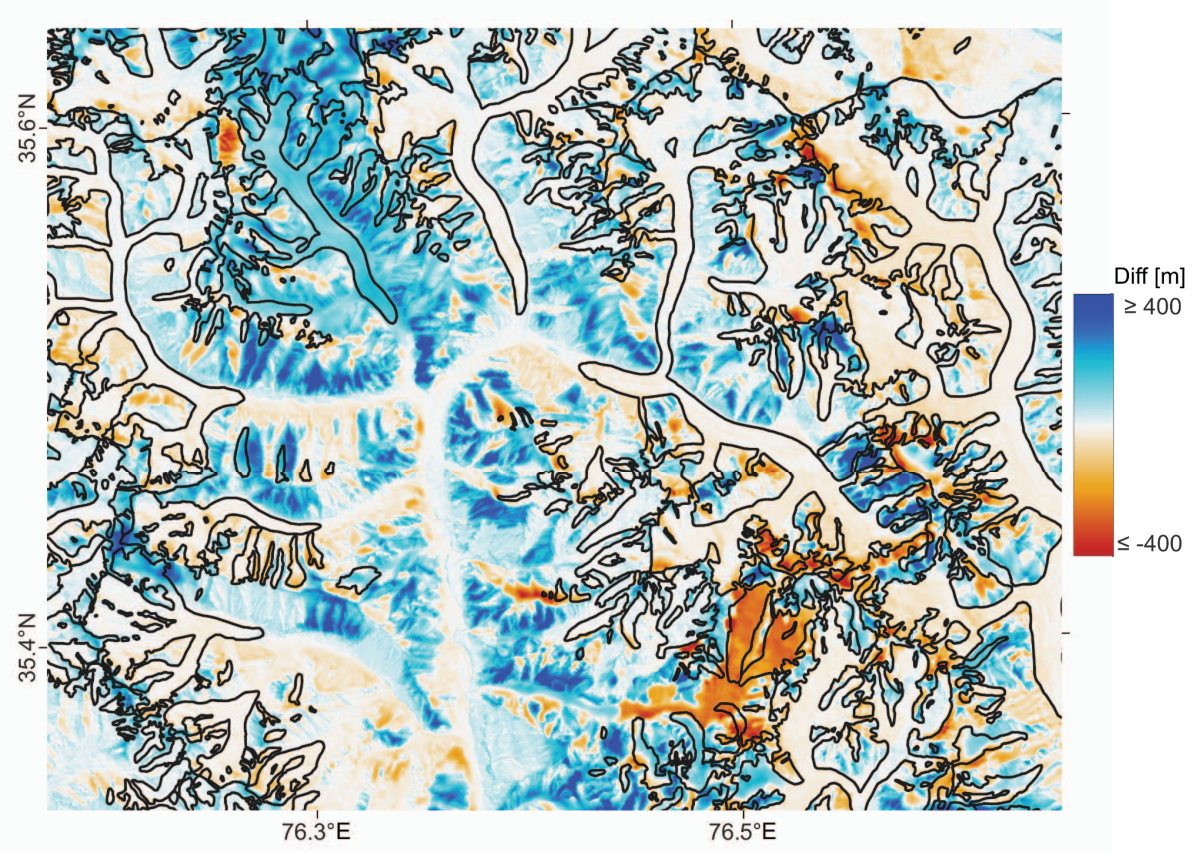

Figure 3.2.2: Differences between Copernicus GLO-30 DEM and the SRTM DEM v4.1 over a subset of the Karakoram in metres. Glacier outlines of the RGI 7.0 (black lines) are overlaid.

The impact of the different atmospheric parameterisation and of using different DEMs on the spectral reflectances has been investigated by executing the atmospheric and topographic correction processing step for a selected satellite scene with changing each only one variable, and calculating afterwards the difference per spectral band. The tests were performed for the Sentinel-2 tile T43SFV of 21 July 2022 using:

1) different DEMs (GLO-30 - SRTM v4.1), and
2) different atmospheric parameterisations (user defined - standard mid-latitude summer).
The histograms of the resulting difference maps for the spectral bands at 1.6 μm, 833 nm and 665 nm are shown in Figure 3.2.3.

Overall, the impact of the DEM on the resulting spectral reflectances is small. Nevertheless, for many regions in cast shadowed areas, the difference in the spectral reflectances is in the order of 0.05 to 0.20 which has a significant impact on the following processing steps. For clear sky observations, the impact of using a user defined atmospheric parameterisation versus a standard atmosphere depends on the spectral band, but is small compared to the other identified error sources.

All auxiliary data have to be prepared in the same UTM/WGS84 map projection, spatial extent and grid spacing as the satellite image used for the product generation.

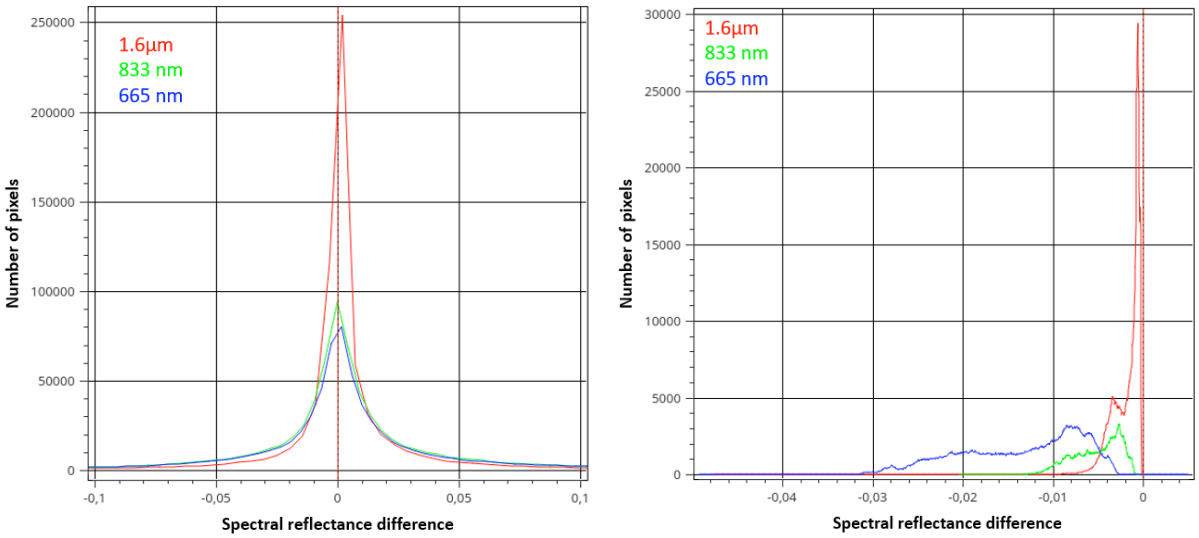

Figure 3.2.3: Differences in the spectral reflectance of the Sentinel-2 bands 11 (1.6 µm), 8 (833 nm) and 4 (665 nm) after executing the atmospheric and topographic correction changing each only one variable- Left: using different DEMs (GLO-30 - SRTMv4.1), each with the same user defined atmospheric parameterisation; right: using different atmospheric parameterisation (user defined - standard mid-latitude summer), each with the GLO-30.

Algorithms used in the data pre-processing and for the cloud masking

The pre-processing of the satellite data to correct the acquisitions for atmospheric and topographic effects can introduce some uncertainties depending on the settings of the atmospheric parameterisation, the correct identification of cast shadowed areas, and the combination of the atmospheric fluxes resulting from the radiative transfer model and the cast shadow estimation. The uncertainty of this pre-processing step depends also on the spectral band and its sensitivity to particular atmospheric parameters.

A major source of uncertainty is linked to the masking of clouds over glaciated areas. Sensor specific approaches are used to identify clouds:

- Sentinel-2 MSI: open-source python module "s2cloudless" (https://github.com/sentinel-hub/sentinel2-cloud-detector)
- Landsat 4 – 9 TM / ETM+ / OLI(-2) / TIRS(-2): cloud mask attached to scene in QA_PIXEL data set, resulting from adapted FMask

For both sensors, the performance of the cloud screening can vary significantly from one acquisition to the next. Thus, the uncertainty from the cloud mask on the GLF product remains unknown and random. In the worst case, clouds have to be masked manually.

Classification of glacier facies

The GLF classification is based on a hierarchical decision tree considering scene-dependent thresholds applied to a combination of spectral bands from the visible to the shortwave infrared spectral range. Each classification step is linked to some uncertainty, and is building additionally on the integrated uncertainties described before.

Considering only the atmospheric and topographic correction and the glacier facies classification, uncertainties are in general higher for pixels identified as cast shadowed glacier areas than for illuminated pixels. The correct classification of firn areas on glaciers and the separation of these areas from bright ice areas is still a major source for uncertainty.

3.2.3 Other uncertainties

The GLF product provides a binary classification of four glacier surface types: 1) snow on glaciers, 2) clean glacier ice, 3) debris covered glacier areas, and 4) firn areas or bright ice areas. Any observed mixed pixel information on glaciers is classified in only one of these surface types, and is thus linked to some uncertainty.

Cloud shadows are not yet handled in an automated way, as an accurate cloud mask is required as pre-condition. Any glacier areas affected by cloud shadows might thus be affected by misclassifications, which are also not yet properly reflected in the uncertainty estimation.

3.3 Glacier surge detection

3.3.1 Major error sources

We anticipate the following major error sources for the detection of surges based on radar backscatter differences between subsequent years. These error sources are in detail also discussed and exemplified in Leclercq et al. (2021) and Kääb et al. (2023).

Visual interpretation. The detection of surges is based on visual interpretation by an operator (Fig 3.3.1). Whereas for most surges the backscatter signal is clear and unambiguous, some surges show signals that can be misinterpreted, i.e. falsely interpreted as surges or overseen and omitted. Also, clear surge signals can be overlooked when the operator misses to check all glacier areas of the region of interest.

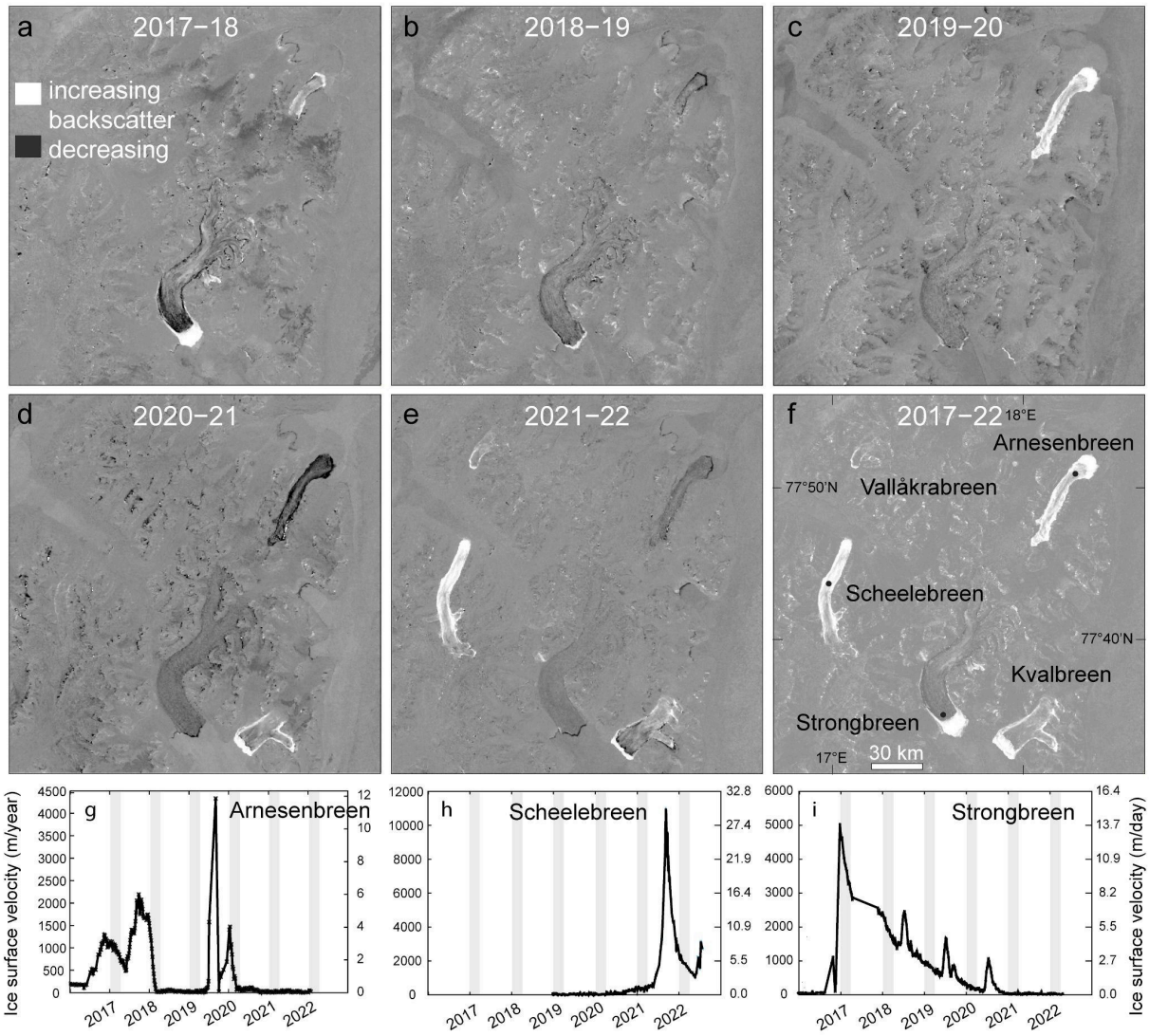

Fig 3.3.1: Examples of winter-to-winter Sentinel-1 radar backscatter changes for a region in south-east Spitsbergen, displayed as normalized differences between maximum winter backscatter of two subsequent years (a-e). Bright greyscale indicates increasing backscatter, dark greyscale decreasing backscatter over time. Increasing backscatter is interpreted as increasing crevassing and surge-type activity, and vice-versa. The middle right panel (f) shows the maximum backscatter normalized difference over the entire five-year period and indicates the five surges observed in the area. The lowest row (g-i) shows selected comparisons to glacier surface velocity time series. The grey vertical bars in the panels of the lowest row indicate the periods over which Sentinel-1 data have been stacked for examples a-f (1 Jan – 1 Apr of each year). Velocity series g-i refer to single points on the surge centre (black dots in panel f).

Weak and complex changes in glacier surge backscatter

Closely linked to potential errors from the visual interpretation are surges that by their nature do not produce clear changes in backscatter or where other changes coincide with backscatter changes from surging. Most but not all glacier surges express themselves in development in heavy crevassing but crevassing might be not clearly visible due to, for example, debris cover or snow cover. Typically the disappearance of crevasses (connected to surge termination) gives a less clear signal than the appearance of crevasses at surge start. An example is provided in Fig. 3.3.2.

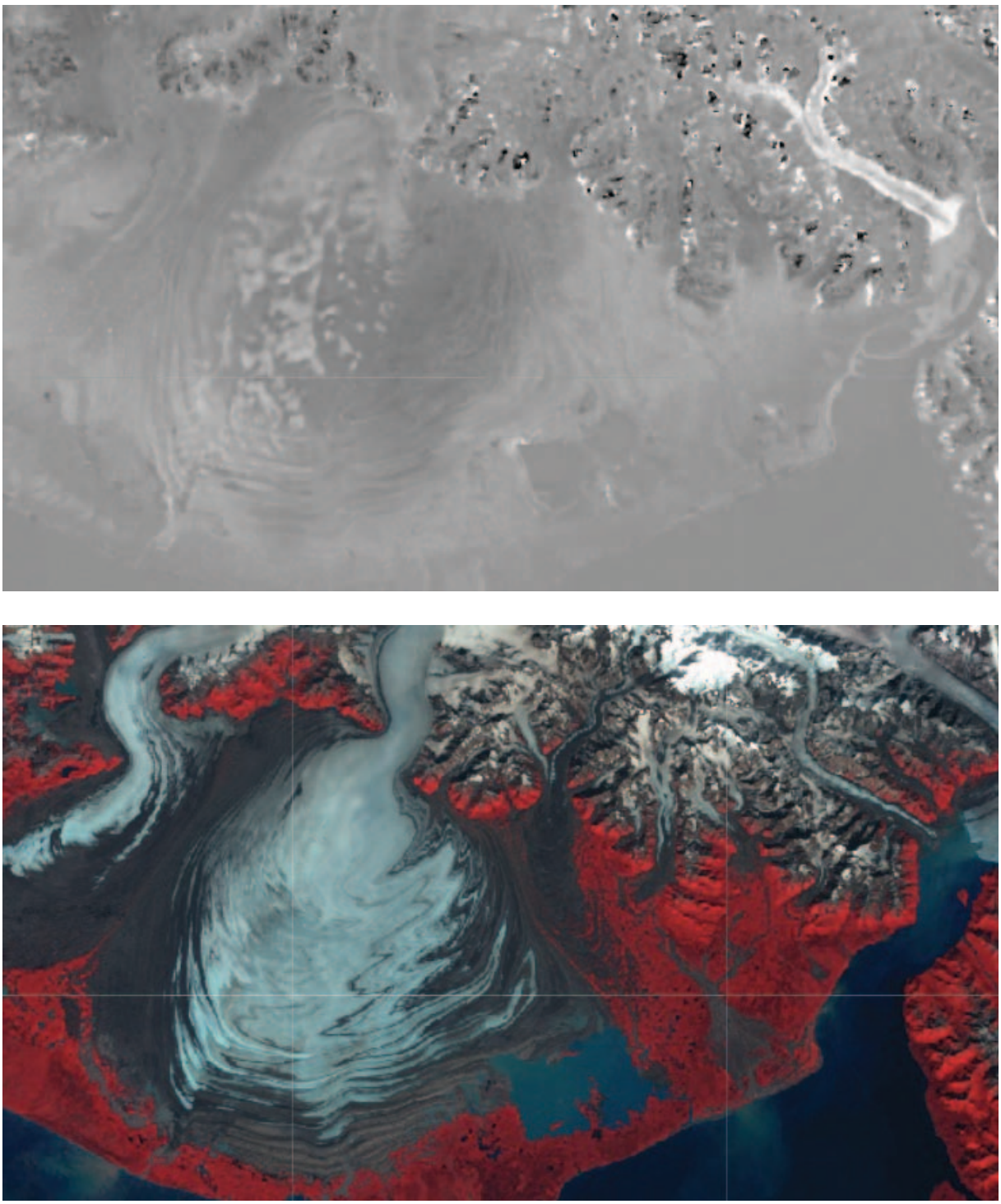

Fig 3.3.2: Malaspina Glacier, Alaska. Top: Sentinel-1 backscatter differences; bottom: Landsat image. The crevasse changes associated with a surge-like acceleration of Malaspina glacier (image centre) are only weak, compared with the Turner glacier surge to the upper right of the images.

Spurious surge-like backscatter changes. Similar to the previous topic, backscatter changes sometimes resemble surge patterns but have a different origin. Typical examples include snow/firn melt patterns, (snow) avalanches or uplift/subsidence of glacier parts due to ice-marginal lakes (example in Fig. 3.3.3).

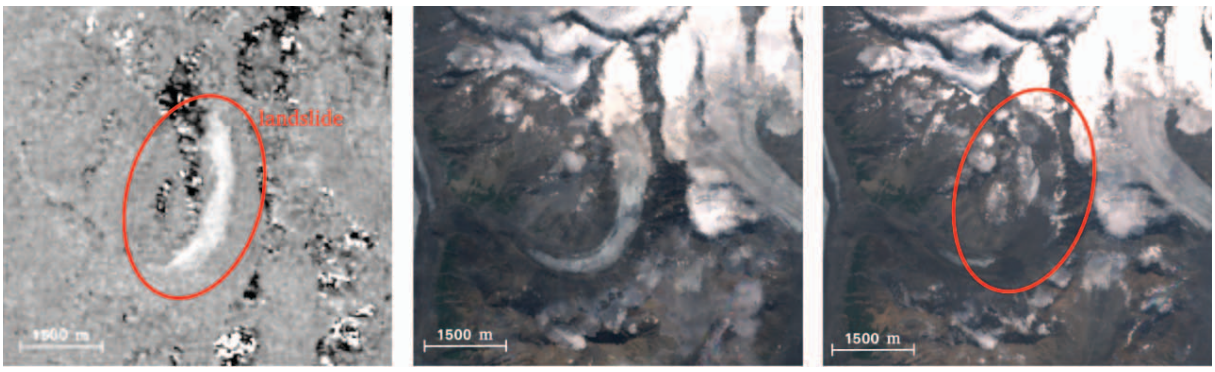

Fig 3.3.3: Example of a landslide that creates a backscatter signal that spuriously resembles a surge. Left: Sentinel-1 based backscatter changes; middle and right: Landsat images before and after the landslide running over a glacier.

Topographic effects. Standard topographic effects in SAR data such as layover or foreshortening cause problems for detection and interpretation of surges in valleys with steep flanks. These effects complicate surge detection in particular when they are combined with weak and complex surge backscatter changes as the example in Fig. 3.3.4 shows.

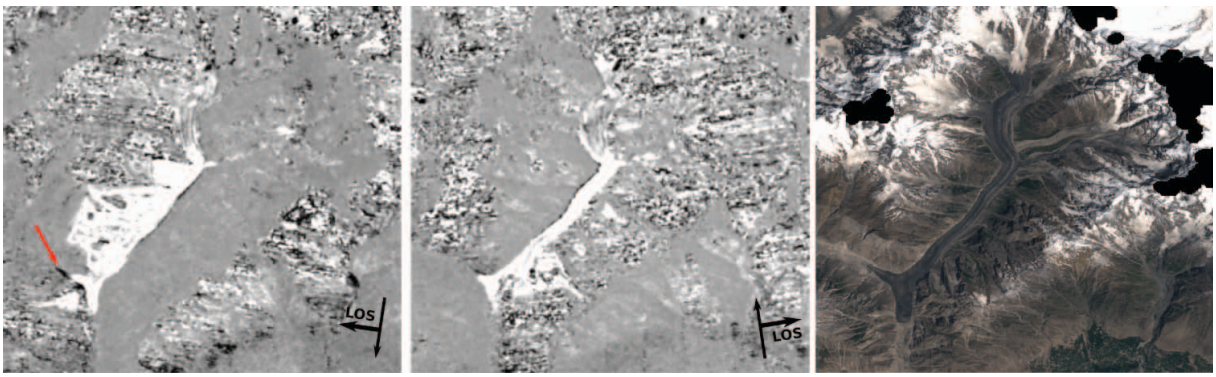

Fig 3.3.4: Topographic effects on backscatter images of the Shispher Glacier surge, Karakorum. Left: descending Sentinel-1; middle: ascending Sentinel-1; right: Landsat. Red arrow indicates a temporary glacier-dammed lake.

3.3.2 Uncertainties per processing step

Image pre-processing. During the pre-processing of the SAR images, complicating effects can mainly originate from errors in georeference of individual data and from errors in topographic correction. Very occasionally in Google Earth Engine for example, Sentinel-1 scenes can be shifted with respect to their correct georeference. This confuses the stack processing that the visualisation of backscatter changes is based on. Errors in the DEM used for topographic correction lead to horizontal location errors (the effect of which can be avoided by only stacking and comparing data from the same nominal orbit).

Stacking. The stack statistics that are used to produce seasonal backscatter signals to be compared between years are sensitive to georeference errors (see above) and strong overall backscatter variations in the area of interest, e.g. from rainfall or melt events during winter which normally is a period of comparably stable backscatter.

Visual surge detection and interpretation. Once differences between backscatter stack statistics (e.g. max or 90% percentile) of different years are available, the further process is based on visual detection and interpretation by an expert operator. As described above the potential error sources are thereby:

- Overlooking of individual surges or entire glaciated areas
- Weak or complex backscatter (change) patterns of actual surges
- Spurious surge-like backscatter (change) patterns of glaciers that do not surge
- Topographic SAR effects (radar layover, foreshortening, shadow)
- Overlay/combination of two or more of the above error sources

3.3.3 Other uncertainties

The main underlying uncertainty in the detection of surges from SAR backscatter changes stems from the unclear definition of what a glacier surge is. Definitions of surges based on observations depend so far mainly on the observation and detection method used. There is no clear and unambiguous definition available (and likely not helpful for practical purposes).

It is important to stress that our definition of surge-type activity is based on backscatter changes and does thus not necessarily agree with other definitions used for surge-type activity and other indicators. Our approach appears to coincide well with large changes (most clearly with increases) in ice speed (Leclercq and others, 2021), visual interpretations of enhanced crevassing in optical images, and glacier advances due to surges, which typically also become visible in the approach of this study.

We find two main reasons for uncertainty between surge classification in our approach and classifications based on ice speed variations. Guillet and others (2022), for instance, involve ice speed changes in assigning surge characteristics and use the amplitude of intra-annual speed variations relative to the average long-term ice speeds, in addition to at least one other indicator from peculiar elevation changes and visual surge indications. This approach includes many comparable slow and long-lasting surge-like processes, a type of ice-flow instability that our backscatter approach typically is not sensitive to as it detects mainly large changes between subsequent years. (A future implementation of our approach could look into multi-year backscatter changes or backscatter variations within the entire Sentinel-1 stack instead of annual stacks). The difference in approaches by us and Guillet et al. and thus the different surge indications applied is not only a methodological one, but it reflects also a fundamental range in surge definitions in terms of amplitude and duration of (speed) changes that are certainly open to discussion, including the definition of when a surge starts and ends.

Features such as looped moraines or specific landforms in the glacier forefield, often used for the identification of surge-type glaciers, indicate past surge activity rather than ongoing one. By design, the approach to detect surges from backscatter changes cannot detect such retrospective indicators. Similarly, our kinematic approach cannot detect specific patterns of elevation change that can be associated with surge-type activity, such as build-up of accumulation zones during the quiescent phase or drainage of accumulation zones and thickening of tongues during the surge active phase (Guillet and others, 2022). Our approach is thus different, and potentially complementary, to other (semi-)automatic approaches of surge characterisation and mapping. Herreid and Truffer (2016), for instance, use deformations of moraine features to find and characterise glacier speed variations. On the substantive surges that we map such features are typically destroyed, if present at all. On the other hand our approach is not well suited to detect more subtle surge-like processes. Vale and others (2021) support

their surge identification by detection of particularly large glacier length changes. As surge-related terminus advances are often accompanied by terminus crevassing, our approach is also able to detect such processes. Our inherent surge definition does however not directly encompass glacier advance (or retreat) as an indicator. On the other hand, our approach works also for surges that do not involve glacier length changes, such as tributary surges.

4. References

CLS, ECMWF, isardSAT, LEGOS, MSSL, NOVELTIS and PML (2021): S3MPC STM Annual Performance Report - Year 2021, https://sentinels.copernicus.eu/documents/247904/3519647/S3MPC.CLS.APR.010+-+i1r0+-+STM+Annual+Performance+Report+-+Year+2021.pdf

European Space Agency (2022): Copernicus Sentinel-3 STM Thematic Products 2nd Test Data Set, https://sentinels.copernicus.eu/fr/web/sentinel/-/copernicus-sentinel-3-stm-thematic-products-2nd-test-data-set/

Herreid, S. and Truffer, M. (2016): Automated detection of unstable glacier flow and a spectrum of speedup behavior in the Alaska Range. *Journal of Geophysical Research-Earth Surface*, 121(1), 64–81; https://doi.org/10.1002/2015jf003502

Gourmelen, N., Escorihuela, M. J., Shepherd, A., Foresta, L., Muir, A., Garcia-Mondéjar, A., Roca, M., Baker, S.G. and Drinkwater, M.R. (2018): CryoSat-2 swath interferometric altimetry for mapping ice elevation and elevation change. *Advances in Space Research*, 62(6), 1226–1242. https://doi.org/10.1016/j.asr.2017.11.014

Guillet, G., King, O., Lv, M., Ghuffar, S., Benn, D., Quincey, D. and Bolch, T. (2022): A regionally resolved inventory of High Mountain Asia surge-type glaciers, derived from a multi-factor remote sensing approach. *The Cryosphere*, 16(2), 603–623;

Hall, D.K., Bayr, K.J., Schöner, W., Bindschadler, R.A., and Chien, J.Y.L. (2003): Consideration of the errors inherent in mapping historical glacier positions in Austria from ground and space (1893–2001). *Remote Sensing of Environment*, 86, 566–577; doi.org/10.1016/S0034-4257(03)00134-2

Kääb, A., Winsvold, S.H., Altena, B., Nuth, C., Nagler, T. and Wuite, J. (2016): Glacier Remote Sensing using Sentinel-2. Part I: Radiometric and geometric performance, application to ice velocity. *Remote Sensing*, 8, 895; https://doi.org/10.3390/rs8070598

Kääb, A., Bazilova, V., Leclercq, P., Mannerfelt, E. and Strozzi, T. (2023): Global clustering of recent glacier surges from radar backscatter data, 2017–2022. *Journal of Glaciology*, 1-9; https://doi.org/10.1017/jog.2023.35

Leclerq P., Kääb A. and Altena B. (2021): Brief communication: Detection of glacier surge activity using cloud computing of Sentinel-1 radar data. *The Cryosphere*, 15, 4901-4907.

Noh, M.-J. and Howat, I.M. (2015): Automated stereo-photogrammetric DEM generation at high latitudes: Surface Extraction with TIN-based Search-space Minimization (Setsm) validation and demonstration over glaciated regions. *GIScience & Remote Sensing*, 52(2), 198–217; https://doi.org/10.1080/15481603.2015.1008621

Prats, P., Rodriguez-Cassola, M., De Zan, F., Scheiber, R., Lopez-Dekker, P., Barat, I. and Geudtner, D. (2015): Role of the Orbital Tube in Interferometric Spaceborne SAR Missions. *IEEE Geoscience and Remote Sensing Letters*, 12 (7), 486-1490; https://doi.org/10.1109/LGRS.2015.2409885. ISSN 1545-598X

Rengarajan, R., Storey, J.C. and Choate, M.J. (2020): Harmonizing the Landsat ground reference with the Sentinel-2 Global Reference Image using space-based bundle adjustment. *Remote Sensing*, 12(19), 3132; https://doi.org/10.3390/rs12193132

Vale, A.B., Arnold, N.S., Rees, W.G. and Lea, J.M. (2021): Remote detection of surge-related glacier terminus change across High Mountain Asia. *Remote Sensing* 13(7), 1309; https://doi.org/10.3390/rs13071309

Williams, R.S. Jr., Hall, D.K., Sigurdsson, O. and Chien, J.Y.L. (1997): Comparison of satellite-derived with ground-based measurements of the fluctuations of the margins of Vatnajøkull, Iceland, 1973–92. *Annals of Glaciology*, 24, 72–80.

5. Acronyms

ALOS	Advanced Land Observing Satellite
DEM	Digital Elevation Model
ECV	Essential Climate Variable
GCP	Ground Control Point
ICESat	Ice, Cloud, and land Elevation Satellite
InSAR	Interferometric SAR
LOS	Line Of Sight
RADAR	Radio Detection and Ranging
RGI	Randolph Glacier Inventory
RMSE	Root Mean Square Error
SAR	Synthetic Aperture Radar
SLC	Single Look Complex